Climatology of Anomalous Propagation Radar Echoes in a Coastal Area

Mesnard F., Henri Sauvageot

Climatology of Anomalous Propagation Radar Echoes in a Coastal Area

FRÉDÉRIC MESNARD

Laboratoire d'Aérologie, Observatoire Midi-Pyrénées, Université Paul Sabatier, Toulouse, and Institut Universitaire de Technologie de Tarbes, GEII, Université Paul Sabatier, Tarbes, France

HENRI SAUVAGEOT

Laboratoire d'Aérologie, Observatoire Midi-Pyrénées, Université Paul Sabatier, Toulouse, France

(Manuscript received 17 November 2009, in final form 29 April 2010)

ABSTRACT

Anomalous propagation (AP) of ground-based radar beam results in the detection of ground echoes beyond the horizon. One year of data gathered with an S-band meteorological radar located on the coast in southwest France is used to analyze the spatial distribution of AP ground echoes (APE). The APE distributions of duration and reflectivity in the radar-observed area are found to be strongly related to the main feature of the regional orography and topography up to the farthest distance (250 km) observed by the radar, notably the nature of the surface, the topographic orientation with respect to the radar beam direction, and the altitude. The distribution of APE in the studied area is found to be strongly anisotropic around the radar, with wide differences between land and sea. Rain accumulation equivalent to the APE is, in certain places, of the same order or higher than the real rain depth. The distribution of the ground surfaces, as calculated from a ground numerical model, compares qualitatively well with the APE radar reflectivity distribution.

1. Introduction

For surface-based radars, nonstandard tropospheric refraction (e.g., Ulaby et al. 1982) can result in anomalous propagation (AP). The most obvious, or perceptible, consequence of AP is the detection of surface echoes at all distances from the radar, notably beyond the geometric horizon. AP is associated with a distortion of radar ray direction (that is of antenna beam shape) with respect to the propagation conditions of the standard atmosphere (Ulaby et al. 1982) referred to as the standard propagation, and thus AP affects echo distributions and, possibly, some radar equation parameters, such as the antenna radiation pattern, which are assumed to be constant.

Distribution of temperature and water vapor vertical gradients in a radar-observed area depends on climatic conditions and atmospheric circulation. Configuration and nature of the surface (in relation to short- and longwave radiative transfers), temperature, and evaporation are important for AP, as illustrated, for example, by Babin (1996), Brooks et al. (1999), Bech et al. (2000, 2002), Steiner and Smith (2002), Mentes and Kaymaz (2007), and Lopez (2009). AP phenomena are thus of interest for climatological characterization of an area.

Numerous studies have investigated and discussed various aspects of the physics of the AP phenomenon, such as ducting conditions and duct distributions (depth, height, intensity) (the bibliographical background of the paper is given in section 2). However, the duct climatology at a single point does not account for occurrence and distribution of AP echoes (APEs). The reason is that, in most cases, ducting conditions are not correctly observed because of a lack of temperature and water vapor resolution of measurements (usually radiosondes) that does not permit the capture of the thin atmospheric structure. Another reason is that using a vertical profile at one point to describe the ducting conditions over a radar-observed area assumes that the atmosphere is homogeneous horizontally (as a one-dimensional structure) and isotropic around the radar, which is not at all a realistic assumption. The horizontal extent of the ducts has never been clearly documented and discussed. Similarly, the duration of ducting conditions has not been documented. The APs, and thus the AP-associated atmospheric

Corresponding author address: Dr Frédéric Mesnard, Université Paul Sabatier, Laboratoire d'Aérologie, Observatoire Midi-Pyrénées, 57 avenue d'Azereix, BP 826, 65007 Tarbes, France.
E-mail: mesf@aero.obs-mip.fr

DOI: 10.1175/2010JAMC2440.1

conditions, frequently have a transitory and sporadic character. Temperature and water vapor profiles at wide time intervals (twice a day for radiosonde network observations) thus do not enable its capture. The uncertainty induced by the spatiotemporal variability of refractivity on the measurements of the reflectivity field is not quantified.

A way (that no one seems to have documented) to approach the observation of ducting consequences on radar propagation is to consider the information conveyed by the cumulative distribution of AP surface echoes. It is the object of this paper to present and discuss the information contained in the climatology of the AP surface echoes. An overview of the anomalous propagation phenomenology is given in the next section. The experimental dataset is described in section 3, and an introductory example of APE is presented in section 4. The space–time distribution of APE and the distribution of the APE radar reflectivity factor are addressed in sections 5 and 6, respectively.

2. Anomalous propagation: An overview

a. Refraction

For surface-based radar propagation at quasi-horizontal beam elevation, the sensitive terms are the vertical gradients of air temperature and water vapor. The quantity used to describe and discuss the microwave propagation is the refractivity N, a particular form of the refractive index n used because n is close to unity for the air. For radio frequencies between 1 and 100 GHz, the refractivity can be approximated with the simplified expression

$$(n-1)\times 10^6 = N = \frac{77.6p}{T} + \frac{37.3\times 10^4 e}{T^2}, \qquad (1)$$

where p is the total atmospheric pressure (hPa), e is the water vapor partial pressure (hPa), and T is the temperature (K) (e.g., Bean and Dutton 1968).

Let α be the angle of the radar ray with the surfaces of constant N, and let us consider an arc ds along a radar ray. Let us denote $d\alpha$ as the corresponding variation of the angle of the tangent to this ray. The curvature of this ray is C and the radius of curvature ρ with $C = 1/\rho = d\alpha/ds$. Bean and Dutton (1968) show, from simple geometrical consideration, that the radius of curvature is related to the vertical gradient of refractivity dN/dz where z is the vertical coordinate, by the relation

$$\frac{1}{\rho} = -\frac{1}{n}\frac{dN}{dz}\cos\alpha \times 10^{-6}, \qquad (2)$$

with ρ in meters if z is in meters.

For an elevation close to zero, it can be written

$$\frac{1}{\rho} \approx -\frac{dN}{dz}\times 10^{-6}.$$

Relation (2) shows that radar rays bend toward the medium of higher refractivity. In the standard atmosphere, at low tropospheric levels, refractivity decreases with altitude and radar rays bend downward (Fig. 1). For the standard atmosphere, $dN/dz = -0.04\ \mathrm{m}^{-1}$ corresponding to the standard refraction. In this case, for $\alpha = 0$, $\rho = 25\ 000$ km and the rays horizontally transmitted move away from the earth's surface. For $dN/dz = -0.157\ \mathrm{m}^{-1}$, the radius of curvature of horizontally transmitted rays is equal to that of the earth's surface ($\rho_e \approx 6371$ km). Usually, four modes of propagation are distinguished (e.g., Bean and Dutton 1968; Gossard 1977; Skolnik 1980; Pratte et al. 1995; Babin 1996; Steiner and Smith 2002; Lopez 2009). The normal refraction, including the standard one, is for dN/dz between 0 and $-0.079\ \mathrm{m}^{-1}$ corresponding to rays bending downward with ρ larger than ρ_e. The three other modes are called nonstandard or AP, namely the subrefraction when $dN/dz > 0$ corresponding to rays bent upward; the superrefraction when dN/dz is between -0.079 and $-0.157\ \mathrm{m}^{-1}$, corresponding to rays bent more than normal but less than the earth's surface; and the trapping or ducting when $dN/dz < -0.157\ \mathrm{m}^{-1}$. In this last case, ground returns can be observed at the distance where the radar beam reaches the earth's surface. These ground returns are the so-called AP echoes. Of course, APEs are different in nature from the short-distance ground clutter echoes detected by the main or secondary lobes of the radar antenna beam along the line of sight propagation.

Only the transmitted rays with an elevation inferior to about 1°, that is, nearly parallel to the duct, can be trapped, as illustrated, for example, by Steiner and Smith (2002) and Lopez (2009). All the rays making up a radar beam do not have the same elevation angle (because of beam divergence) and thus are not necessarily refracted in the same way. Consequently, the radiation pattern of a radar beam may be modified by anomalous propagation. Notably, in case of ducting, only parts of the beam may be ducted. Moreover, vertical refractivity profiles are not necessarily homogeneous along the horizontal direction (e.g., at the transition between land and sea), therefore the validity of $N(z)$ observed at a particular location is questionable elsewhere inside a radar-observed area.

b. Duct formation

It is usual, in radar propagation studies, to consider, for practical purposes, the modified refractivity M, which includes the effect of earth's curvature (Bean and Dutton 1968). Here M is given as

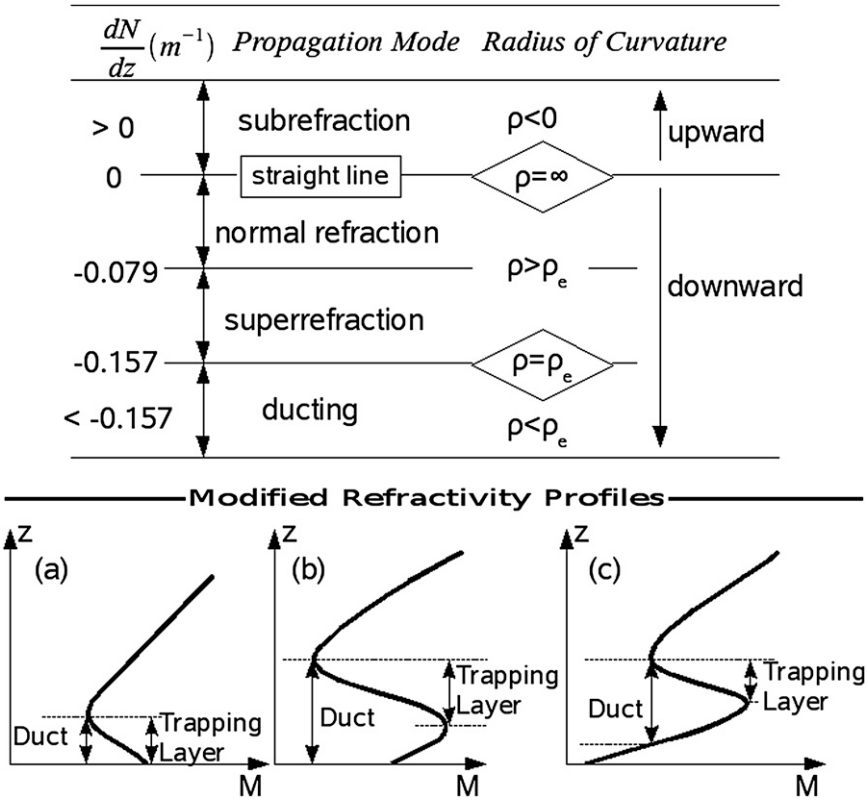

FIG. 1. (top) Propagation modes and radius of curvature for rays emitted with zero elevation. Here ρ_e is the earth radius. (bottom) Modified refractivity profiles showing the main types of ducts: (a) surface duct, (b) S-shaped surface duct, (c) elevated duct (after Turton et al. 1988).

$$M = N + \frac{z \times 10^6}{\rho_e}, \tag{3}$$

where z is the height above sea level (m) and ρ_e is the earth's radius (m); that is,

$$\frac{dM}{dz} = \frac{dN}{dz} + 0.157. \tag{4}$$

Ducting, or radar beam trapping ($\rho < \rho_e$) occurs for $dM/dz < 0$ (cf. Fig. 1). Following the definition of Turton et al. (1988), a trapping layer is located inside and at the top of a duct. The duct is defined as the layer in which M is higher than the minimum value at the top of the trapping layer. It can be thicker than the trapping layer. Trapping layers and ducts are easily identified form the vertical profiles of M. Figure 1 shows the three main types of ducting profiles: Fig. 1a is an evaporative surface duct, Fig. 1b is a surface S-shaped duct, and Fig. 1c an elevated duct (duct with bottom higher than ground level). Of course, real M profiles can be a combination of these three main types, with, possibly, several ducts at various heights or several trapping layers inside a same duct.

As emphasized by Skolnik (1980), water vapor gradients are more effective than temperature gradients alone in the creation of ducts. Strong negative gradients of N associated with ducts are created in layers where T increases while e decreases with height, that is, with ground radiative cooling. This happens when the sun elevation is low and during clear-air nights, particularly in summer above moist ground. Over sea, radiative cooling is not as strong as over land and ducts are mainly created above the surface by evaporation. Evaporation ducts are common over sea, notably when warm air from the land is advected above a cool water surface. Some surface ducts, notably over the oceans, are extremely shallow (a few meters). Ground-based ducts (or surface ducts) and evaporation ducts are more common than elevated ducts. Elevated ducts are observed in relation, for example, with warm air flowing above cooler and moister air producing a temperature inversion with water vapor decreasing with altitude.

Anomalous propagation may also be associated with the divergence above the surface of cool air of convective storm downdrafts. At the transition between cool, dense, dry air spreading over the surface and the warm,

damp air located above, sharp gradients are created leading to short-lived AP echoes or to specular reflection.

With the exception of convective storm ducting, APEs are mainly observed in fair weather conditions. APEs are thus more frequent in summer than in winter and in tropical areas than at mid- and higher latitudes. Of course it does not occur in well mixed atmospheres, notably in the presence of low stratiform clouds.

c. Climatology and occurrence

Propagation within an atmospheric duct has some similarity to that within a waveguide with preferential modes of propagation and a critical wavelength below which propagation is not ducted (Kerr 1951; Skolnik 1980; Turton et al. 1988; Brooks et al. 1999). It has been suggested (Kerr 1951; Skolnik 1980) that the maximum wavelength (λ_{max}) that can be propagated in a surface duct of intensity dN/dz is related to the depth of the duct (d) by the simplified approximate formula

$$d = \left[\frac{\lambda_{max}}{2.5}\left(-\frac{dN}{dz}\times 10^{-6}\right)^{-1/2}\right]^{2/3}, \qquad (5)$$

with d, λ_{max}, and z in the same units. With $dN/dz = -0.157\ m^{-1}$, Eq. (5) predicts that the duct must be at least 10 and 22 m to propagate wavelengths of 3 and 10 cm, respectively. Clearly, relatively thin layers with strong gradients may cause anomalous propagation. Ducts can overlap; that is to say, thin duct can be enclosed (embedded) within a thicker one.

Several authors have discussed the climatology of ducts to document the distribution of their features. Babin (1996), using a wide sample of refractivity profiles observed with an instrumented helicopter off the Atlantic coast near Wallops Island, Virginia, gives a climatology of surface ducts. Refractivity parameters and ducting are analyzed by Craig and Hayton (1995) over Europe with standard radiosonde data, by Brooks et al. (1999) over the Persian Gulf with instrumented aircraft, by Bech et al. (2000, 2002) over a coastal site around Barcelona in Spain with high resolution radiosondes, by Steiner and Smith (2002) from 16 years of operational radiosondes over the United States, by Mentes and Kaymaz (2007) from two years of radiosonde data over the Istanbul area, and by Lopez (2009) for global climatology from 5-yr European Centre for Medium-Range Weather Forecasts (ECMWF) analyses.

Fabry et al. (1997) and Fabry (2004) show that ground target observation can be used to retrieve low-level refractivity distribution and that the refractivity field exhibits some potentialities for mapping near-surface water vapor distribution (Weckwerth et al. 2005). This approach is valid for directly detected nearby ground echoes, not for AP ground echoes.

Comparison of duct features available in the literature is not easy for various reasons. The main reason is that most measurements were performed with different techniques that have sampling specifications not adapted for observation of thin atmospheric structures such as duct, notably space and time resolution, as well as sensitivity. In addition, these specifications are not the same and sometimes not clearly described in the various quoted references. Most studies use synoptic network standard radiosonde data on availability grounds. Standard synoptic radiosondes with two profiles a day and vertical sampling resolution at low levels not better than several tens of meters only provide a lower bound of occurrence for the deepest ducts, as noted by Steiner and Smith (2002).

The available literature shows that duct climatology displays important differences from site to site and is, in part, specific for each site. Values of annual occurrence percentage of surface duct are observed between 21% by Craig and Hayton (1995) over Europe and 85% for Bech et al. (2000) over the Mediterranean. They are 20% throughout most of the United States and larger than 30% for Southern California and most of the eastern seaboard states (Steiner and Smith 2002). They are 31% with higher frequency in summer than in winter over Istanbul (Mentes and Kaymaz 2007). Most authors find that the duct depth has a maximum occurrence between 10 and 40 m and is thinner in winter than in summer. Values quoted for duct strength are between -2 and $-6\ m^{-1}$ (e.g., Mentes and Kaymaz 2007). Values for depth of surface duct (that is vertical distance between the surface and the upper limit of duct) are found to range from few meters to several hundred meters (e.g., mean duct depth of 412 m in Bech et al. 2000). Other aspects such as horizontal extent, duration, or overlapping of ducting structure are only qualitatively mentioned.

AP echoes are a cause of bias for quantitative precipitation estimation from automatic radar data processing. That is why various techniques have been proposed to mitigate ground clutter and AP echoes among meteorological data: for example, a statistical filtering of pulse-to-pulse signal fluctuations (Tatehira and Shimizu 1978, 1980; Aoyagi 1983), texture-based techniques (Moszkowicz et al. 1994; Gabella et al. 1999; Upton and Fernandez-Durán 1999; Haddad et al. 2000), image correlation filter and Doppler filtering (Doviak and Zrnic 1993; Pratte et al. 1995; Seltmann and Reidl 1999), polarimetric radar techniques (Giuli et al. 1991; Ryzhkov and Zrnic 1998; da Silveira and Holt 1999), and fuzzy logic algorithm (Berenguer et al. 2006; Cho et al. 2006;

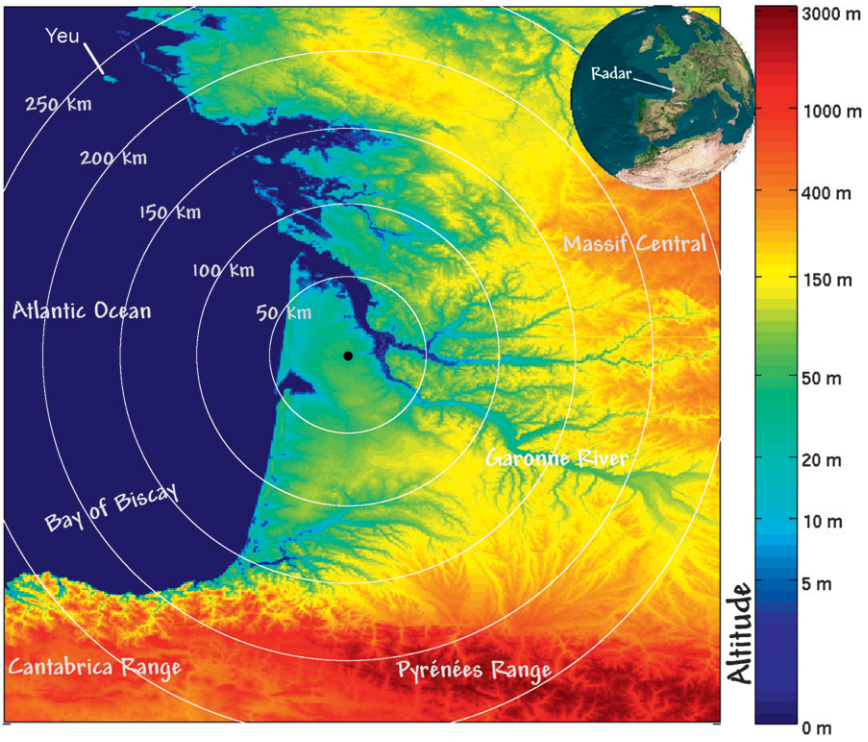

FIG. 2. Map showing the relief of the observed area. Circles are range markers from the Bordeaux-Mérignac radar (black point). Colors represent altitude in meters as indicated by the color bar.

Gourley et al. 2007). A review of the literature on this topic is given by Steiner and Smith (2002), who propose the use of the three-dimensional reflectivity structure gathered at various elevations in volumetric scan.

The above overview led to the conclusion that the spatiotemporal duct structure cannot be considered to have been satisfactorily documented and understood. It does not seem possible to deduce the APE distribution at one time from the ducting structure deduced from a one-site vertical temperature and water vapor profile. It is thus pertinent and informative, in order to better know the local AP problem, to consider and discuss the cumulative distribution of AP echoes, which is the subject of the present paper.

3. Data

The data used for this study were collected with a radar of the French operational meteorological radar network. This radar is located at Bordeaux-Mérignac (44°49′53″N, 00°41′28″W, altitude 50 m) in southwestern France, near the Atlantic coast (Fig. 2) on the top of a tower of 20-m height (i.e., the radar is 70 m MSL). The climate of the Bordeaux area is of maritime type. Most of the rainy events are zonal frontal cyclonic disturbances moving eastward, from sea toward land, with the general circulation at midlatitude. The climatic conditions are mostly homogeneous although, during the summer season, the frontal systems are often reduced to the convective line associated with the cold-frontal line. The mean annual rainfall is about 800 mm evenly distributed throughout the year. The Bordeaux area (Fig. 2) is flat; within a radius of 150 km around the radar, the surface altitude is below 200 m, except in the northeast, between azimuths 40° and 80°, at a distance of more than 130 km, where the first hills of the Massif Central, with an altitude below 400 m, are located. About 200 km south of Bordeaux is the Pyrenees Range, with several summits reaching an altitude of 3000 m, at the border between France and Spain. Westward, the Pyrenees Range merges with the Cordillera Cantabrica, a line of mountains with an altitude below 2000 m, forming the southern limit of the Bay of Biscay. This orography is associated with a meridional gradient of the annual rainfall total accumulation over southwestern France, with values increasing up to 1600 mm over the Pyrenees Range. In summary, the interest of the radar area of Bordeaux-Mérignac for an AP distribution study is the availability of sea, flat land, and a significant orography in the same radar-scanned domain.

On a clear-air day, the coastal strip inside the observed area experiences a sea–land breeze circulation. The penetration of sea breeze landward does not exceed 10–20 km from the coast-line (Sauvageot and Despaux 1996). The distribution of rainfall parameters over the Bordeaux area has been analyzed in detail by Nzeukou and Sauvageot (2002) from the radar data of 1996. They have shown that the average rainfall distribution displays a sea–land and a north–south gradient. The structural characteristics of rain fields over the Bordeaux area have been studied by Mesnard and Sauvageot (2003).

To describe the APE reflectivity field, the same quantity as the one employed for precipitation is used, that is the equivalent radar reflectivity factor Z expressed in $\text{mm}^6\ \text{m}^{-3}$ or in dBZ [see definition, e.g., in Sauvageot (1992)]. Calculation of Z assumes that the target is rain, satisfying the Rayleigh approximation, homogeneously distributed inside the radar resolution volume. Using Z enables an easy comparison of the reflectivity levels.

The radar of Bordeaux-Mérignac operates in S band (wavelength $\lambda = 10$ cm), with a 4-m parabolic antenna (half power beamwidth $\theta = 1.8°$), a pulse repetition frequency of 300 Hz, with pulse duration of 2 μs, and peak power of 700 kW. The scanning mode is CAPPI with elevation $\alpha = 1.5°$ for radial distances $r < 50$ km and $\alpha = 0.5°$ for $r \geq 50$ km. The sampling interval is 5 min; therefore, every 5 min a Cartesian image of 512×512 pixels of 1×1 km^2 is recorded. The number of steps for Z digital coding is 54 beginning at 9 dBZ. The minimum detectable Z at 200 km is 15 dBZ, which corresponds approximately to rain rate R of 0.2 mm h^{-1}. The radar is calibrated to provide correct values of the radar reflectivity factor Z.

For this study, one year of data, that is 105 120 CAPPIs of 5 min, were considered. All the CAPPIs were visualized to extract those displaying APEs without precipitation echoes. Identification of APEs on radar images are easily performed by a trained operator, notably by considering an animation over several successive images. Such an animation displays prominent differences in motion, texture, and reflectivity variation (see section 4). In brief, for APEs observed with a non-Doppler, non-polarimetric radar, the reflectivity gradients associated with the cellular structure of rain fields are replaced by the texture of the ground. The textural structure is not advected. The change with time is modified with a blinking of some parts of the echo areas and a longer correlation time of the signal fluctuation. The dependence in distance (r) is closed to inverse third power of r. There is no tridimensional structure, anomalous propagation disappears when the beam elevation increases above 1° or 2° (see the references given in section 2c about the techniques of APE suppression). After this sorting, there remain about 21 000 images with APEs in clear-air conditions, representing 20% of the time or about 72 days. Images with AP in the presence of rainy echoes represent about 2% of the time. It rains over the Bordeaux area about 10% of the time. The year used, 1996, has been retained among others without particular reason.

The meteorological station of Bordeaux-Mérignac launches radiosondes (RS) twice per day, at 0000 and 1200 UTC for the world meteorological watch. These RS data were tentatively used to analyze the occurrences of ducting over the region. It was concluded that RS at Bordeaux-Mérignac cannot be usefully related to the observed AP distribution because of a lack of resolution (approximately 100 m; Babin 1996; Steiner and Smith 2002) and spatial validity for the 500-km diameter of the radar-observed area. These results are not presented.

4. Introductory example of APE

As an introductory observation to illustrate the APE variability in space and time, Fig. 3 presents the field of ground echo continuous duration observed between 1815 and 2130 UTC 17 June 1996. The distribution mapped at the time t displays the continuous duration before t of APEs present at t. At 1815 UTC, ground clutter echoes are detected close to the radar. These echoes are present all the time as will be shown in section 5. APEs begin to appear at radial distances larger than 200 km from the radar, over the Cantabrica Range at the location of high reliefs. At 1915 UTC, sand hills along the coastline are detected. Then APEs increase in area and duration. However, the distribution does not evolve homogeneously. The contours of the APE instantaneous area and reflectivity distributions (not presented) change at each scan. The radial at approximately 225° azimuth over the ocean is due to interference from the Bilbao (Spain) radar (see section 5) and is observed only in the 2000 UTC scan. The Yeu Island, at 245 km in the 330° azimuthal direction, is detected at 2130 UT. All that proves that the ducting conditions around the radar are not isotropic and homogeneous and that they are not stable in time. They move. The change in the time of the refractivity distribution can be assumed to be controlled by a local evolution of the atmosphere such as the one linked to the diurnal cycle of the radiative balance, or by an advection of the atmosphere, or by a mixing of the two processes in a proportion that varies with time.

5. Space–time distribution

a. Cumulative AP echo duration distribution

Figure 4a presents the 1-yr cumulative AP echo duration (CAPED) distribution in the studied area; that is, at each pixel of the CAPPI, the total number of

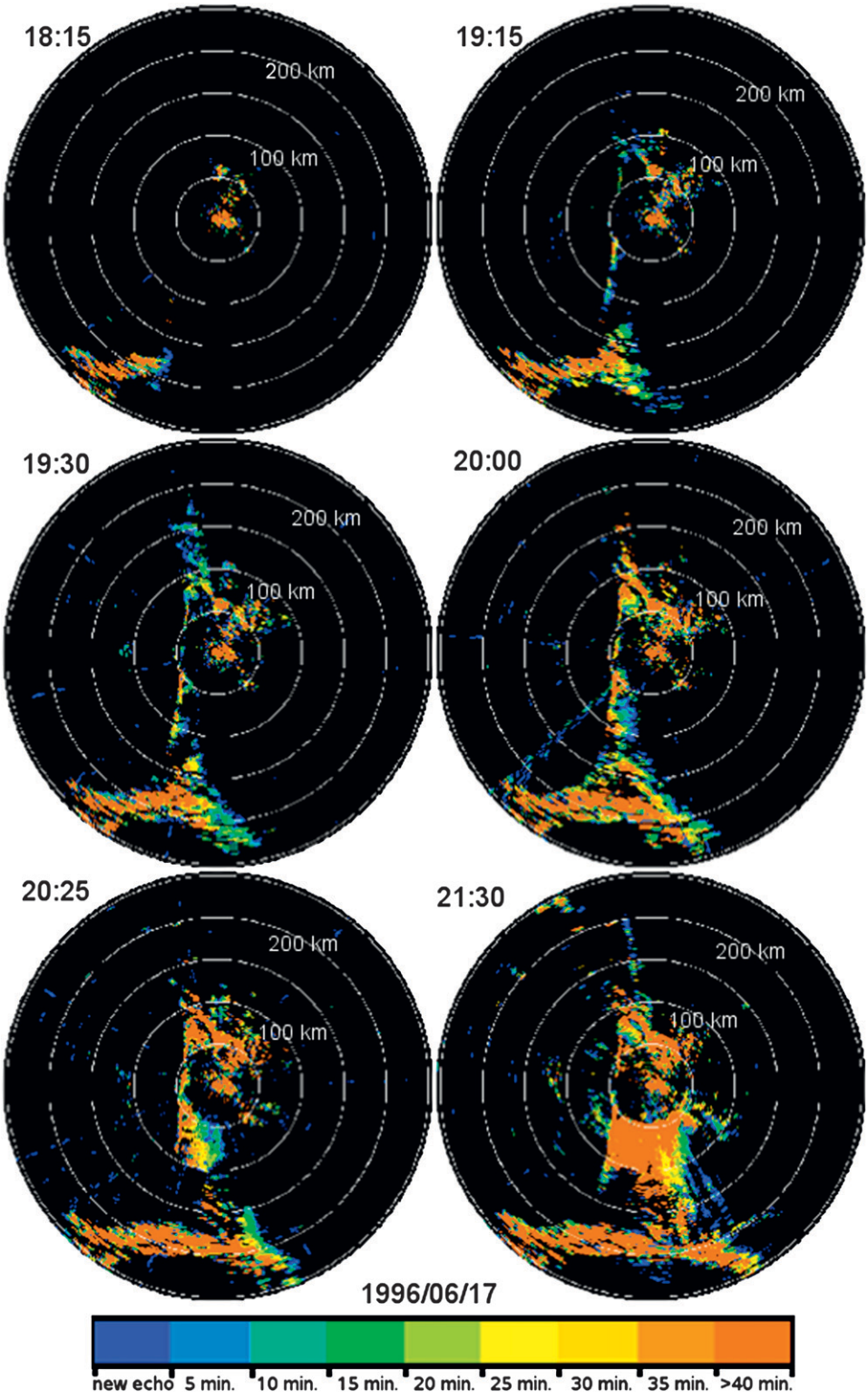

FIG. 3. Evolution of APEs between 1815 and 2130 UTC 17 Jun 1996. Colors on the figure are related to the continuous echo duration at the time (min) of the distribution mapping.

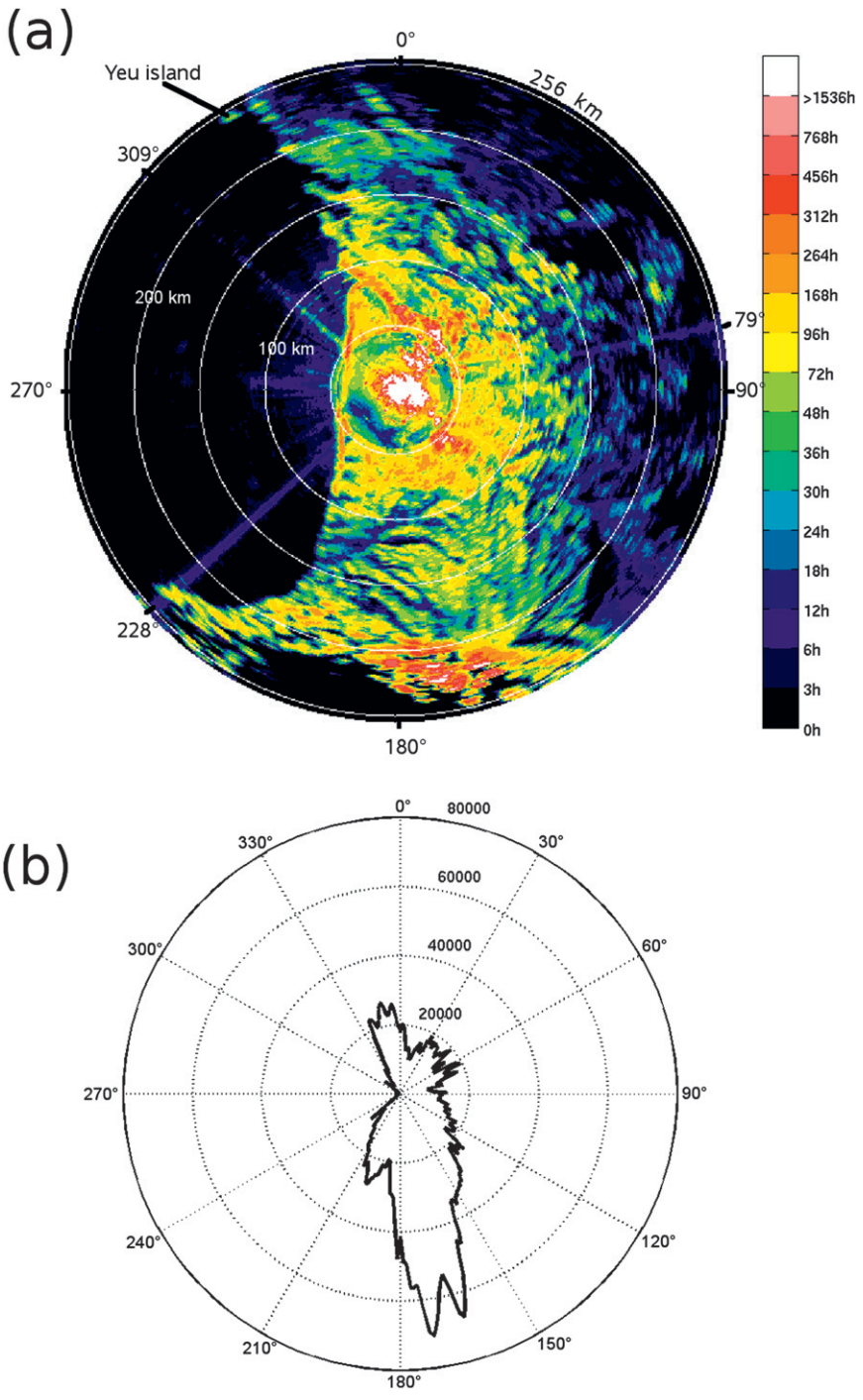

FIG. 4. (a) Cumulative APE duration distribution over the whole year 1996. Colors represent duration in hours as indicated by the color bar. (b) Polar (i.e., radially integrated) representation of the cumulative APE duration distribution around the Bordeaux-Mérignac radar. Circles are labeled in hours and azimuthal directions in degrees.

observations with $Z \geq 15$ dBZ multiplied by the sampling time interval of 5 min.

At a 50-km distance from the radar, a strong discontinuity of echo duration is observed in relation with the change of the CAPPI scan beam elevation (from 1.5° to 0.5°), notably in the southwest direction. Close to the radar, echoes are permanent because some ground echoes are directly detected (along straight lines of sight) by

the radar. Thus, inside the first CAPPI circle ($r < 50$ km), there is mixing of ''direct'' echoes and AP echoes that are difficult to differentiate. That is why this area is not considered in the present analysis. However, it is maintained (not blanked) in the next figures to enable comparison with the other parts of the studied area. For the area with $r > 50$ km, that is, the second CAPPI circular area ($\alpha = 0.5°$), there is no possibility of straight-line ground detection; all echoes are AP echoes.

In some azimuthal directions ($\varphi = 79°$, 228°, 270°, and 309°), radial anomalies are observed. Such anomalies are very usual in radar plan position indicators (PPI). Anomalies along 270° and 309° are linked to the spurious detection of echoes through a partial reflection of the radar beam from a specular reflector close to the radar such as a wall or a pylon. (partial or total blocking, cf. section 6). In the presence of such specular reflection, the distribution of reflectivity along the radius is the one observed in the direction in which the radar beam is deflected. For the radius along $\varphi \approx 228°$ and $\varphi \approx 79°$, the radial homogeneity of the signal suggests another cause independent of the distance such as a source of S-band microwave radiation. As a matter of fact, the Spanish meteorological S-band radar of Bilbao is 250 km away in the 228° azimuthal direction. Ducting of the Bordeaux radar beam in azimuth 228° enables passive detection of the transmission from the Bilbao radar. Ducting of the Bilbao radar beam in the direction of the Bordeaux radar can lead to the same result. The same is in the 79° azimuth with an S-band meteorological radar of the operational network located at Grèze 150 km away from the Bordeaux radar.

What appears clearly by comparing Figs. 2 and 4a is that the CAPED is strongly correlated with the orography over the observed area. CAPED in a pixel can be between zero minutes or several tens of days. Several main factors contribute in a variable proportion to the CAPED. Among them, three can be identified in Fig. 4a.

1) The nature of the surface. The reflection coefficient depends upon surface and subsurface parameters (conductivity and permittivity, roughness, vegetation, etc.; e.g., Ulaby et al. 1982). This influence is obvious through the differences of echo over sea and over land. The sea surface acts as a specular reflector. Cumulative time over sea is smaller than a few hours. It should not be forgotten that the radar is 70 m MSL and that its beam can be unaffected by some ducting conditions linked to low-level sea surface refractivity profiles.
2) Orientation of topographic structures with respect to the radar beam orientation. Valleys, river beds and banks, and crest lines, as well as the shadow areas they create for the radar rays, appear, on Fig. 4a, strongly dependent on their orientation. For example, the small river beds located between 100 and 200 km south of the radar with an east–west direction are associated with shadow lines of almost zero CAPED, but the deep valley of the Garonne River, stretching radially northwest–southeast of the radar, has no shadow effect for $r < 200$ km. Another example is the line of sand hills stretching along the north–south part of the Atlantic coast. Their altitude, except for some particular points, is very low (under 20 m), but their CAPED is very high. However, it decreases as the angle between their direction and the radar beam decreases, notably for $\varphi < 200°$.
3) Altitude. The highest CAPEDs are observed over the Pyrenees Range, particularly over their central part, between azimuth 160° and 190°, for distance between 200 and 260 km. The location of CAPED maximum areas corresponds to the highest summits made up of rock, which is ice-covered in some places. Maximum summit altitude is around 3300 m. At that distance (around 250 km), for a standard refractivity vertical profile, a ray emitted at 0° elevation from Bordeaux is about 0.6 km above the higher summits. A small bending of the radar beam is enough to have echoes from these summits. It is worth noting that the small island of Yeu with a maximum altitude of 30 m, located in azimuth 330° and at a distance of 245 km, is detected. Other factors are discussed below.

Figure 4a shows that the CAPED distribution contains significant information of climate interest in relation with radar propagation. It notably enables estimation of the time fraction a particular point at the surface is seen by the radar because ducting is affecting the associated radar propagation. Figure 4a also shows that the extent of the CAPED distribution along the east–west direction is different (narrower) than the one in north–south direction. To objectively emphasize this point, Fig. 4b shows the polar distribution of the CAPED around the radar (along each radial direction, the CAPED of the pixels were added). The diagram is strongly anisotropic because of the low-duration echoes over the sea and long-duration echoes over the Pyrenees.

b. Mean and maximum continuous duration distribution

The continuous duration of an APE in a pixel is the time during which an APE is observed without interruption in this pixel with the 5-min sampling interval of the radar. The mean continuous duration distribution of APEs over the year, represented in Fig. 5a, is very similar to the CAPED shown in Fig. 4a, notably the

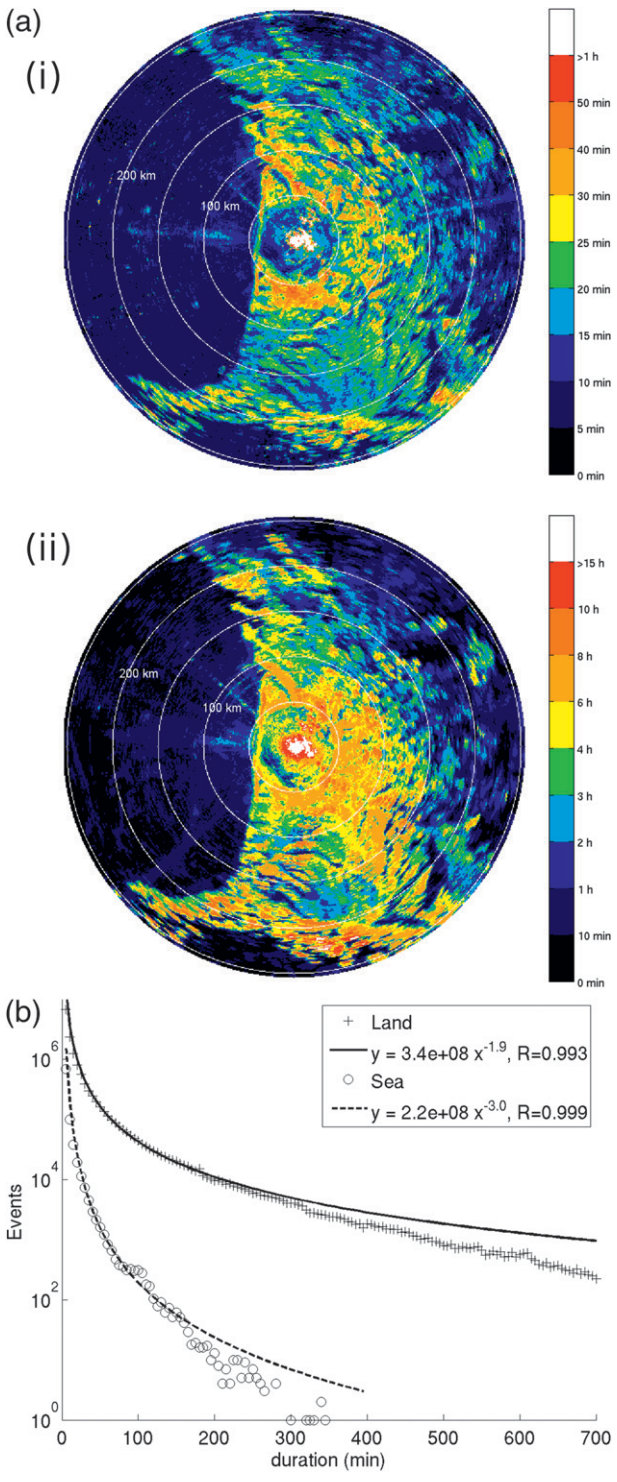

FIG. 5. (a) Duration of continuous observation of APEs averaged over the year 1996. Colors represent duration in minutes as indicated by the color bar. (b) Maximum duration of continuous observation of APEs over the year 1996. Colors represent duration in hours as indicated by the color bar. (c) Frequency distribution of APE continuous duration over the year 1996. The R is the correlation coefficient between the observed distribution and the fitting curve.

north bank of the Gironde (the hill of Médoc), north of the radar, the area between 50 and 70 km south of the radar, and the Pyrenees Range. In the southeast, between 150 and 200 km, there are two sites (Fig. 5a) with a mean duration higher than 45 min surrounded by an area with a mean duration lower than 20–25 min. These peak areas are linked to exceptional long-lasting ducting conditions along the southeast direction from the radar that occurred on 22 and 23 October 1996.

The distribution of the maximum of the continuous duration of APEs (Fig. 5b) surprisingly shows that some APEs can be observed without interruption for more than 10 h. Such long continuous durations are associated with the strong and stable temperature inversion observed in stationary anticyclonic conditions. Differences between Figs. 5a and 5b show that the processes involved in APE are strongly not linear.

The frequency distribution of the continuous duration of APE (Fig. 5c) displays an approximately negative power shape with a slope steeper for sea than for land. APEs are less frequent and of shorter duration over sea than over land. The differences between land and sea APE duration and the relation with reflectivity are discussed in section 6.

6. Distribution of the APE radar reflectivity factor

Figure 6 displays the arithmetic mean of the radar reflectivity factor ($\overline{Z}$) calculated over the whole dataset; in each pixel, the summation of all PPI observations with $Z \geq 15$ dBZ divided by the number of observations (a strong echo appearing only once among the 21 000 PPI observations is represented with a higher $\overline{Z}$ than a permanent echo having a low reflectivity factor).

a. Over the sea

In the $\overline{Z}$ field (Fig. 6), APEs that were not present in Fig. 4 (i.e., corresponding to low CAPED) appear over the sea. Over the sea, the texture of the $\overline{Z}$ field is different from the one over land; it is dotted with some straight-line-shaped patterns (e.g., inside the elliptic contours in Fig. 6). The dots can have a strong reflectivity with $\overline{Z} > 26$ dBZ. An analysis of AP echoes over the sea, with animation from PPIs at 5-min time step, shows that most of these echoes are moving punctual (i.e., smaller than the radar pulse resolution) objects, mainly boats. Individual punctual boat echoes are represented as small arcs of circle centered on the radar. Of course, the arc aperture is related to the antenna beam radiation pattern (2° for the 3-dB beamwidth of the Bordeaux radar). The animation of long-lived continuous AP sequences shows that some arcs of circle move at

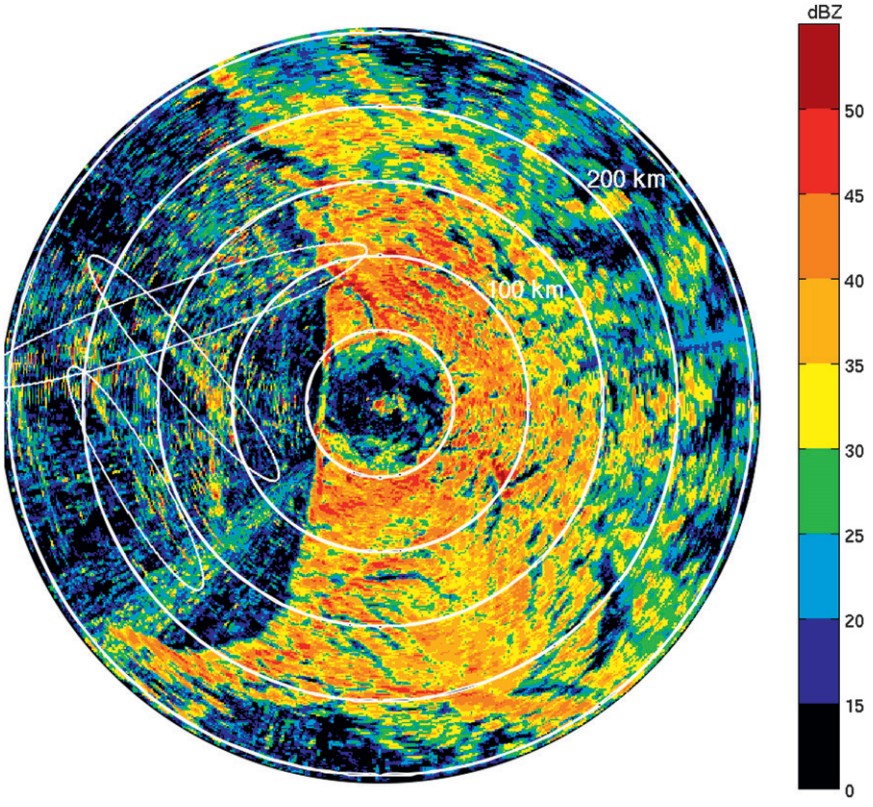

FIG. 6. Distribution of $\overline{Z}$ the radar reflectivity factor of APEs averaged over the year 1996. Black (<15 dBZ) corresponds to no data. Colors represent radar reflectivity factor (dBZ) as indicated by the color bar. Ellipses locate the straight lines assumed to correspond to moving boats.

the velocity of a boat, others are almost fixed. If a boat is motionless (fishing) or if the ducting is of short duration, the boat echo appears as a dot. If the boat is moving during a ducting of long duration, its successive positions generate a line of echoes. For example, the line-shaped pattern inside the elliptic contour between approximately 100 and 200 km, west of the radar, was observed between about 2100 and 2400 UTC 17 June 1996. The target moves northwest over 90.5 km in 2 h and 45 min, that is, with a velocity of about 18 kt (36 km h^{-1}). In fact, there is much maritime activity in the Bay of Biscay (French and Spanish fishing boats and merchant ships in relation to several important fishing and commercial ports). Other kinds of targets such as low-level flying aircraft are a possible but minor source of echo. Around the 228° azimuthal direction, linked to the Bilbao radar detection, a dotted texture is also observed. It is thought that this dotted structure is due to otherwise undetectable boat echoes raised in the $\overline{Z}$ field (>15 dBZ) by the addition of the Bilbao radar-generated background. The moving character of the echoes over the sea explains their low CAPED in Fig. 4a (the boat does not stay a long time in a same pixel). This point appears clearly in Fig. 7 where the CAPED, averaged by class of $\overline{Z}$, as function of $\overline{Z}$, is drawn. It shows that the mean CAPED over the sea is almost independent of $\overline{Z}$ and between 25 and 35 h.

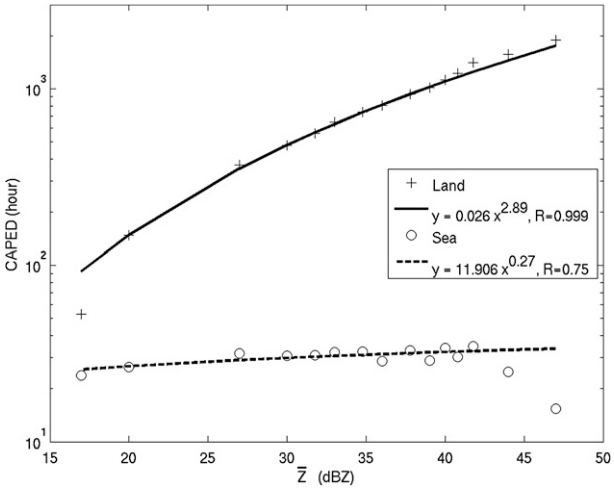

FIG. 7. CAPED as a function of $\overline{Z}$. The R is the correlation coefficient between the observed distribution and the fitting curve.

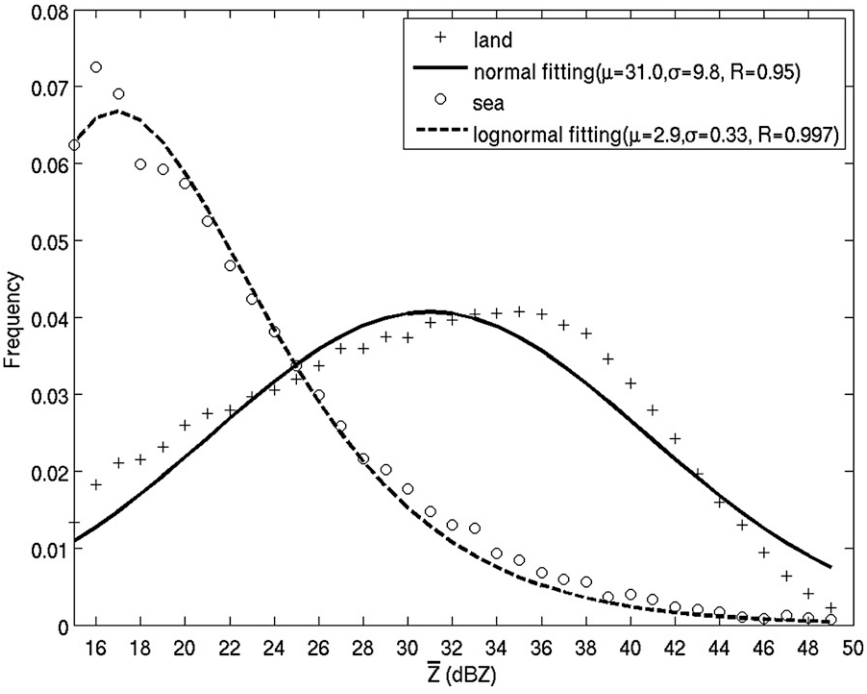

FIG. 8. Probability density function of APE radar reflectivity factor shown in Fig. 6, over the sea and over land. Radial distances <50 km are excluded. The R is the correlation coefficient between the observed distribution and the fitting curve.

b. Over land

Over land, $\overline{Z}$ inside the first CAPPI circle ($r \leq 50$ km) is low because it corresponds to a higher elevation than the second CAPPI circle. For $r > 50$ km, the topography of the $\overline{Z}$ distribution is qualitatively similar to the CAPED distribution because it is determined by ground altitude and shadowed features since, of course, a shadow area of CAPED field is also shadowed in the $\overline{Z}$ field. Figure 7 shows that, over land, CAPED roughly increases with $\overline{Z}$. The curve can be fitted with a power function. Because $\overline{Z}$ is plotted in a logarithmic unit, the distribution in Fig. 6 appears more homogeneous than the CAPED distribution in Fig. 4a. The $\overline{Z}$ spans over 30 dB when the CAPED varies from 100 to 1000 h.

Figure 8 displays the probability density function (pdf) of $\overline{Z}$ over land and over sea. The two curves are strongly differentiated. Over land, the curve is roughly Gaussian and slightly skewed on the right with the mode around 31 dBZ. Over the sea, the curve is strongly truncated on the left with the mode around 17 dBZ.

c. Equivalent rain total accumulation

To estimate the potential bias that APEs can create in rainfall estimation if not identified and removed from the observed radar echo field, the rain total accumulation at ground equivalent to the APEs has been calculated. For the calculation, the midlatitude relation observed in southwestern of France $Z = 228R^{1.62}$ (Sauvageot and Lacaux 1995) was used, with Z in mm^6 m^{-3} and R in millimeters per hour. Results are in Fig. 9. Figure 9a shows, for comparison, the annual rain total calculated from the meteorological echo dataset (i.e., without the APE component) for the year 1996 in the Bordeaux area. The annual rain total is 1 m or more inside the first CAPPI circle ($r < 50$ km) where the permanent direct ground echoes are. It decreases with the distance down to 0 for a radius of about 200 km because of increase with distance of radar beam altitude. This is the kind of pattern usually observed for total rain around a meteorological radar. Over the central part of the Pyrenees Range, some local peak values appear, probably because of an incomplete filtering of APEs in the dataset used for Fig. 9a calculation. Some minimum along the radials in the azimuthal directions 270°, 300°, and 309° are observed because of the masks already pointed out in Fig. 4a. Figure 10b shows the annual rain total equivalent to the APEs calculated with the same Z–R relation, that is to say the bias in rain total radar estimation if APEs were processed as rain echoes. The pattern of Fig. 9b is qualitatively close to the pixel to pixel product of APE duration (Fig. 4a) by $\overline{Z}$ (Fig. 6). In a wide part of the

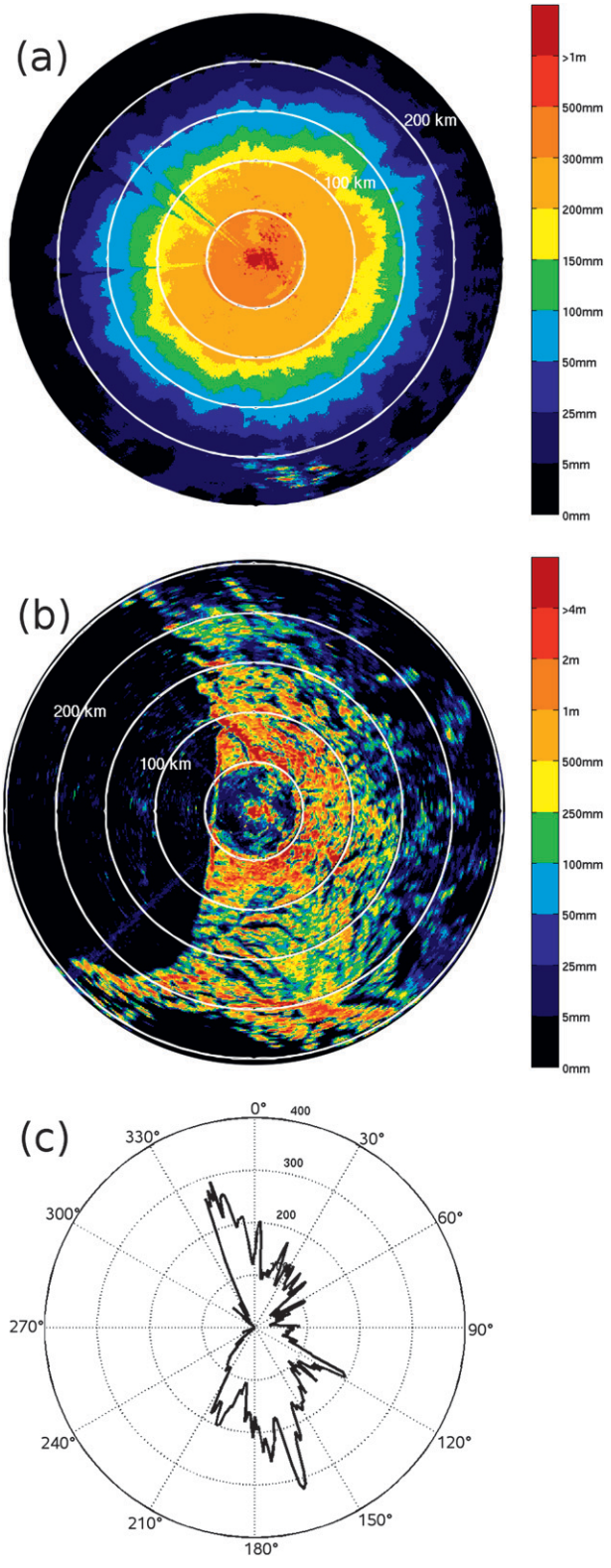

FIG. 9. (a) Distribution of the rainfall total accumulation at ground around the radar estimated from the radar measurements over the year 1996. APEs are removed. Colors represent rain total (mm) as indicated by the color bar. (b) As in (a) but calculated only from the APEs. (c) Polar representation around the radar of the cumulative rainfall height distribution (m) calculated from the APEs ($r > 50$ km).

radar-observed area, the APE equivalent rain is higher than 1 m, that is, higher than the real rain. It is notably the case above the Pyrenees Range and Cantabrica Range. The APE equivalent rain is very anisotropically distributed around the radar. To illustrate this point, Fig. 9c shows the polar diagram of the APE equivalent rain. The APE rain distribution is very heterogeneous spatially, particularly at the limit of the shadowed areas. The APE equivalent precipitation removing is clearly a necessity for hydrological use of radar.

d. Relation with a ground numerical model

In the previous sections, the CAPED and the APE radar reflectivity factor distributions have been shown to be related to the orography. To sharpen this relation, data from a numerical model of ground provided by the Shuttle Radar Topography Mission (SRTM) has been used to construct a virtual image showing the ground surface visible from the radar (Fig. 10). It has been assumed that only the ground surface with the normal included in the RHI plan (P) crossing this surface return a signal. The used SRTM data have a horizontal resolution of 30 s of arc, that is, about 90 m, and a vertical resolution of 10 m. However, the Cartesian pixels of Fig. 10 have a size of 1×1 km^2. The values displayed in the pixels of Fig. 10 are the maximal slope, in the plan (P), observed at the SRTM resolution, inside the 1×1 km^2 pixels. The slopes are not averaged inside the pixels because the relation between the radar return and the ground surface orientation with respect to the incident radar rays is strongly nonlinear (e.g., Skolnik 1980) in such a way that, in the 1×1 km^2 pixel radar return, the maximal value at the SRTM resolution is dominant.

The qualitative relation between CAPED (Fig. 4a) and the APE reflectivity factor distribution (Fig. 6) is clearly strongly increased in comparison with Fig. 2; see notably the line of sand hills along the Atlantic coast and the hydrographic network in the left lower part of the figure, north of the central Pyrenees Range.

7. Summary and conclusions

One year of data gathered with a coastal S-band meteorological radar, located along the Atlantic coast of southwestern France, has been used to analyze the distribution of AP radar echoes in an area of about 250-km radius around the radar. The land part of this area displays a fair diversity in orographic structures, with flat regions and the Pyrenees Range at the south end. APEs in clear-air conditions are observed about 20% of the time.

The cumulative APE duration distribution is found to be strongly related to orography and topography with

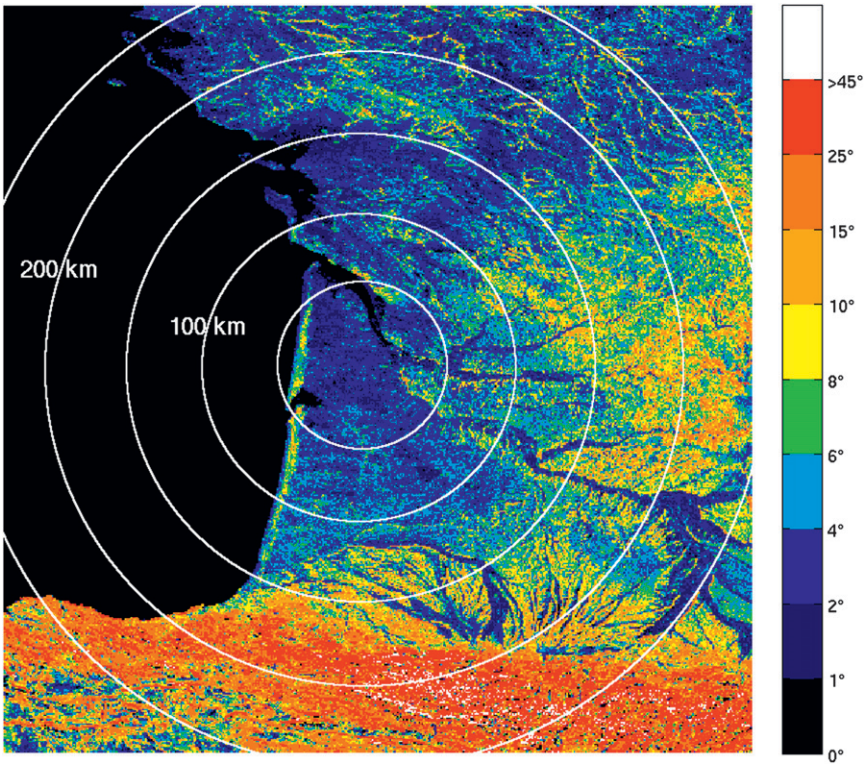

FIG. 10. Distribution of ground surface slopes directed toward the radar and seen by the radar calculated from the numerical model of ground provided by the SRTM. Colors represent the maximal slope in degrees as indicated by the color bar.

duration ranging from 0, for an area shadowed by relief, to more than 1000 h. Contiguity of a relief having a high CAPED with a shadow area having a low or nil CAPED emphasizes this relation. Shadowed areas depend on the direction of the orographic structures, with respect to the radar beam direction. Radial structures are thus weakly bound in the CAPED field. The polar distribution of the CAPED around the radar is strongly anisotropic with a stretch along the north–south direction.

The distribution of the APE radar reflectivity factor reveals, over the sea in the Bay of Biscay, some patterns not appearing in the CAPED field. These echoes and patterns are thought to be mainly due to fishing boats and merchant ships. Over land, the distribution of the mean ($\overline{Z}$) and maximum values of the APE radar reflectivity factors are linked to the orography but also to the nature of the ground radar targets present in each pixel. The CAPED increases with $\overline{Z}$. The probability density function of $\overline{Z}$ is a Gaussian curve slightly skewed on the right with mean around 31 dBZ over land and an unimodal curve truncated on the left with mean around 17 dBZ over the sea.

The distribution of the annual rain total accumulation at the ground equivalent to the APEs is a combination of the CAPED and radar reflectivity distribution. It shows that the APE equivalent rain total polar distribution is strongly anisotropic around the radar. It is, in some pixels, higher than the real rain total. Removing the bias due to APE for radar rainfall measurement is thus necessary.

The distribution of ground surfaces with normal directed toward the radar has been calculated using a ground numerical model. This distribution compares qualitatively very well with the CAPED and with the APE radar reflectivity distribution.

The study of APE distributions presented in this paper demonstrates that, in the observed area, the cause for anomalous propagations, that is to say the structure of the refractivity field around the radar, is, in general, strongly variable over short time and space scales and strongly anisotropic along the azimuthal direction. The case of a long-lived, stable, spatially homogeneous reflectivity field is the exception. This point is important for applications. It emphasizes the fact that radiosondes do not provide data that describe the tridimensional aspect of the refractivity field—in agreement with previous works (notably Steiner and Smith 2002; Fabry 2004; Weckwerth et al. 2005; Fabry 2006).

In summary, the APE duration and reflectivity distributions can be roughly and tentatively described as the superposition of several factors (including factors not discussed in the present paper), namely,

- a factor related to the refractivity distribution along the radar beam;
- a factor depending on the radar system parameters (wavelength, beam shape, transmitted power, polarization, etc.);
- a factor depending on the nature of the surface inside the pixel (including roughness, humidity, vegetation, conductivity and permittivity, presence of structures such as pylon, building, etc.);
- a factor related to the orientation of the topographic structure with respect to the beam direction;
- the altitude;
- the radial distance from the radar;
- a diurnal and a seasonal effect (not studied in the present work because they deserve a specific paper), and possibly others; most of these terms vary independently from each other.

The long-time-averaged APE distributions convey some specificities of a site, notably in relation to electromagnetic propagation, such as

- boundary layer structure and refractivity field;
- forecasting of electromagnetic propagation of microwave frequencies;
- weighting the contribution to APE of each area at the surface in a perspective of mitigation of ground echo disturbances for weather radar applications (sites for wind farms), for sitting of telecommunication antennas, for radioastronomy, etc.;
- correcting cumulative rainfall height.

Acknowledgments. The authors are very grateful to Météo-France for providing freely the data of the Bordeaux-Mérignac radar. They are very appreciative to Dr. Olivier Pujol for science discussions about the anaprop phenomenon.

REFERENCES

Aoyagi, J., 1983: A study on the MTI weather radar system for rejecting ground clutter. *Pap. Meteor. Geophys.,* **33,** 187–243.

Babin, S. M., 1996: Surface duct height distributions for Wallops Island, Virginia, 1995–1996. *J. Appl. Meteor.,* **35,** 86–93.

Bean, B. R., and E. J. Dutton, 1968: *Radio Meteorology*. Dover, 435 pp.

Bech, J., A. Sairouni, B. Codina, J. Lorente, and D. Bebbington, 2000: Weather radar anaprop conditions at a Mediterranean coastal site. *Phys. Chem. Earth,* **25,** 829–832.

——, B. Codina, J. Lorente, and D. Bebbington, 2002: Monthly and daily variations of radar anomalous propagation conditions: How ''normal'' is normal propagation? *Proc. Second European Conf. of Radar Meteorology,* Delft, Netherlands, ERAD Publication Series, Vol. 1, Copernicus GmbH, 35–39.

Berenguer, M., D. Sempere-Torres, C. Corral, and R. Sanchez-Diezma, 2006: A fuzzy logic technique for identifying nonprecipitating echoes in radar scans. *J. Atmos. Oceanic Technol.,* **23,** 1157–1180.

Brooks, I. M., A. K. Goroch, and D. P. Rogers, 1999: Observations of strong radar ducts over the Persian Gulf. *J. Appl. Meteor.,* **38,** 1293–1310.

Cho, Y.-H., G. W. Lee, K.-E. Kim, and I. Zawadzki, 2006: Identification and removal of ground echoes and anomalous propagation using the characteristics of radar echoes. *J. Atmos. Oceanic Technol.,* **23,** 1206–1222.

Craig, K. H., and T. G. Hayton, 1995: Climatic mapping of refractivity parameters from radiosonde data. *Proc. Conf. 567 on Propagation Assessment in Coastal Environments,* Bremerhaven, Germany, AGARD-NATO, 43-1–43-14.

da Silveira, R. B., and A. R. Holt, 1999: A S-band/C-band comparison of the use of polarization for clutter classification in weather radars using neural networks. *Proc. Advanced Weather Radar Systems, Inter. Seminar on COST 75,* Brussels, Belgium, Locarno, European Communities, 758–769.

Doviak, R. J., and D. S. Zrnic, 1993: *Doppler Radar and Weather Observations*. Academic Press, 562 pp.

Fabry, F., 2004: Meteorological value of ground target measurements by radar. *J. Atmos. Oceanic Technol.,* **21,** 560–573.

——, 2006: The spatial variability of moisture in the boundary layer and its effect on convection initiation: Project-long characterization. *Mon. Wea. Rev.,* **134,** 79–91.

——, C. Frush, I. Zawadzki, and A. Kilambi, 1997: On the extraction of near-surface index of refraction using radar phase measurements from ground targets. *J. Atmos. Oceanic Technol.,* **14,** 978–987.

Gabella, M., G. Galli, O. Ghigo, J. Joss, and G. Perona, 1999: Clutter elimination and agreement between hourly precipitation amounts as measured by two radars and a network of gauges. *Proc. Advanced Weather Radar Systems, Inter. Seminar on COST 75,* Brussels, Belgium, Locarno, European Communities, 102–113.

Giuli, D., M. Gherardelli, A. Freni, T. A. Seliga, and K. Aydin, 1991: Rainfall and clutter discrimination by means of dual-linear polarization radar measurements. *J. Atmos. Oceanic Technol.,* **8,** 777–789.

Gossard, E. E., 1977: Refractive index variance and its height distribution in different air masses. *Radio Sci.,* **12,** 89–105.

Gourley, J. J., P. Tabary, and J. Parent du Chatelet, 2007: A fuzzy logic algorithm for the separation of precipitating from nonprecipitating echoes using polarimetric radar observations. *J. Atmos. Oceanic Technol.,* **24,** 1439–1451.

Haddad, B., A. Adane, F. Mesnard, and H. Sauvageot, 2000: Modeling anomalous radar propagation using first-order two-state Markov chains. *Atmos. Res.,* **52,** 283–292.

Kerr, D. E., Ed., 1951: *Propagation of Short Radio Waves*. MIT Radiation Laboratory Series, Vol. 13, McGraw-Hill Book Company, 728 pp.

Lopez, P., 2009: A 5-yr 40-km-resolution global climatology of superrefraction for ground-based weather radars. *J. Appl. Meteor. Climatol.,* **48,** 89–110.

Mentes, S. S., and Z. Kaymaz, 2007: Investigation of surface duct conditions over Istanbul, Turkey. *J. Appl. Meteor. Climatol.,* **46,** 318–337.

Mesnard, F., and H. Sauvageot, 2003: Structural characteristics of rain fields. *J. Geophys. Res.,* **108,** 4385, doi:10.1029/2002JD002808.

Moszkowicz, S., G. J. Ciach, and W. F. Krajewski, 1994: Statistical detection of anomalous propagation in radar reflectivity patterns. *J. Atmos. Oceanic Technol.,* **11,** 1026–1034.

Nzeukou, A., and H. Sauvageot, 2002: Distribution of rainfall parameters near the coasts of France and Senegal. *J. Appl. Meteor.,* **41,** 69–82.

Pratte, J. F., R. J. Keeler, R. Gagnon, and D. Sirmans, 1995: Clutter processing during anomalous propagation conditions. Preprints, *27th Conf. on Radar Meteorology,* Vail, CO, Amer. Meteor. Soc., 139–141.

Ryzhkov, A. V., and D. S. Zrnic, 1998: Polarimetric rainfall estimation in the presence of anomalous propagation. *J. Atmos. Oceanic Technol.,* **15,** 1320–1330.

Sauvageot, H., 1992: *Radar Meteorology*. Artech House, 361 pp.

——, and J. P. Lacaux, 1995: The shape of averaged drop size distributions. *J. Atmos. Sci.,* **52,** 1070–1083.

——, and G. Despaux, 1996: The clear-air coastal vespertine radar bands. *Bull. Amer. Meteor. Soc.,* **77,** 673–681.

Seltmann, J. E. E., and J. Reidl, 1999: Improved clutter treatment within the German radar network: First results. *Proc. Advanced Weather Radar Systems, Inter. Seminar on COST 75,* Brussels, Belgium, Locarno, European Communities, 267–279.

Skolnik, M. I., 1980: *Introduction to Radar Systems*. 2nd ed. McGraw-Hill International Editions, 581 pp.

Steiner, M., and J. A. Smith, 2002: Use of three-dimensional reflectivity structure for automated detection and removal of nonprecipitating echo in radar data. *J. Atmos. Oceanic Technol.,* **19,** 673–686.

Tatehira, R., and T. Shimizu, 1978: Intensity measurement of precipitation echo superposed on ground clutter—A new automatic technique for ground clutter rejection. Preprints, *18th Conf. on Radar Meteorology,* Atlanta, GA, Amer. Meteor. Soc., 364–369.

——, and ——, 1980: Improvements in performance of ground clutter rejection. Preprints, *19th Conf. on Radar Meteorology,* Miami Beach, FL, Amer. Meteor. Soc., 176–179.

Turton, J. D., D. A. Bennets, and S. F. G. Farmer, 1988: An introduction to radio ducting. *Meteor. Mag.,* **117,** 245–254.

Ulaby, F. T., R. K. Moore, and A. K. Fung, 1982: *Microwave Remote Sensing*. Addison-Wesley, 2162 pp.

Upton, G., and J. J. Fernandez-Durán, 1999: Statistical techniques for clutter removal and attenuation detection in radar reflectivity images. *Proc. Advanced Weather Radar Systems, Inter. Seminar on COST 75,* Brussels, Belgium, Locarno, European Communities, 747–757.

Weckwerth, T. M., C. R. Pettet, F. Fabry, S. J. Park, M. A. Lemone, and J. W. Wilson, 2005: Radar refractivity retrieval: Validation and application to short-term forecasting. *J. Appl. Meteor.,* **44,** 285–300.